JOURNAL OF AIRCRAFT
Vol. 42, No. 3, May–June 2005

Simulating the Aerodynamics of the NASA John H. Glenn Icing Research Tunnel

Chirag Bhargava[*] and Eric Loth[†]
University of Illinois at Urbana–Champaign, Urbana, Illinois 61801
and
Mark Potapczuk[‡]
NASA John H. Glenn Research Center at Lewis Field, Cleveland, Ohio 44135

The objective of this study is to develop and employ a numerical simulation strategy for predicting the airflow from the spray bars to the test section of the NASA John H. Glenn Icing Research Tunnel (IRT). In particular, predictions of the mean velocity and turbulence distributions were desired throughout this flow domain to later investigate droplet dispersion. Computational airflow results were produced using the WIND code (developed by NPARC) with a second-order accurate finite difference scheme and the shear stress transport k–Ω urbulence model. The inflow conditions for the flow domain were derived from the IRT measurements just upstream of the spray bars, which reflected the contributions to turbulence from the upstream heat exchanger wake. It was found that inclusion of the spray bar wakes and the air jets (of the spray nozzles) were required to describe the wind-tunnel turbulence distribution. Because it was impractical to simultaneously resolve the overall flow domain (60 ft long), along with the detailed flow around the 10 spray bars and the flow within a hundred air jets (issuing from 1/8-in. nozzle diameters), these features were simulated individually and then algebraically combined together to give an approximate solution. The results of the spray bar wake combined with the heat exchanger flow yielded good prediction of test section mean velocity and turbulence for the jets-off condition. Inclusion of all of the individual air jets also yielded reasonable resulting predictions of mean velocity and turbulence in the test section.

Introduction

THE Federal Aviation Administration's certification of commercial aircraft and military performance assessment requires evaluation during icing conditions. Effective ground-based simulation of icing conditions is conventionally achieved through the use of nozzles on a spray bar system where the water droplets are entrained in the wake of spray bars, transported downstream by the tunnel air, reach a supercooled state from the subfreezing air temperatures, and result in a dispersed cloud at the test section.A primary design consideration of the icing cloud is that the test section liquid water content (LWC) should have high spatial uniformity to mimic realistic atmospheric icing characteristics. Trial and error adjustment of nozzle and test conditions to simulate atmospheric conditions properly is a complex process. Thus, computational methods, which track the turbulent dispersion of the water droplets as they proceed from the nozzles to the test section, could be beneficial in designing and understanding effective testing conditions.

Most previous droplet trajectory methodologies used for icing research tunnels have primarily considered only the mean velocity distributions with the tunnel, for example, Bragg and Khoudadoust.[1] However, it was noted by Hancir and Loth[2] that turbulent diffusion is an important factor that affects the spatial uniformity of the icing cloud. DeAngelis et al.[3] developed a two-phase algorithm that successfully predicted turbulent dispersion of water droplets in the Arnold Engineering Development Center Aero-Propulsion wind tunnel. The procedure was based on a Lagrangian transport methodology for the droplet phase and was used to study key parameters affecting the LWC in the testing section. A parametric study was completed to investigate the effects of computational, spray, vapor, and wind-tunnel parameters. It was found that LWC spatial deviations depend primarily on tunnel turbulence levels and secondarily on droplet temperature and velocity. Based on this technique, Hancir and Loth[2] conducted studies for the pre-1999 configuration of the NASA John H. Glenn Icing Research Tunnel (IRT). Their results indicated that turbulence resulting from the heat exchanger, spray bars, and air jet wakes were all critical factors in modeling the droplet dispersion. Their results also indicated that it was unnecessary to model the wall boundary layers in terms of icing cloud distributions. However, their predictions yielded only qualitative agreement with respect to the measured test section turbulence. The lack of quantitative fidelity was attributed to the lack of well-characterized flow from the complex geometry heat exchanger (which yielded substantial flow uniformities) and to the absence of the detailed flow simulation of the jet and spray bar wake features (because these features were only treated with simple one-dimensional empirical expressions as opposed to being predicted numerically).

The present investigation is a modification and extension of the previous computational research by Hancir and Loth[2] but for the revised NASA Glenn IRT configuration. Wind-tunnel improvements completed in 1999 included replacing the original folded heat exchanger and expanding the width of the tunnel loop to accept the larger flat heat exchanger, as well as adding new corner turning vanes up and downstream of the heat exchanger and exit guide vanes downstream of the drive fan. In particular, there was a replacement of the heat exchanger system to improve the quality and uniformity of the airflow.[4] A portion of the revised tunnel geometry is given in Fig. 1a, which includes spray bars located just upstream of the 14:1 tunnel contraction section. Modifications also included an increase in the number of air/water nozzles shown in Fig. 1b.

The arrangement of the nozzles located at the spray bar trailing edges was obtained after 30 iterations by Ide and Oldenburg[5] to maximize the icing cloud uniformity in the test section. Comparing the experimental data taken before and after the tunnel modifications, it was found that there was a significant improvement

---

Presented as Paper 2003-566 at the AIAA 41st Aerospace Sciences Meeting, Reno, NV, 6–9 January 2003; received 16 April 2003; revision received 7 August 2003; accepted for publication 7 August 2003.

[*] Graduate Research Student, Department of Aeronautical and Astronautical Engineering. Member AIAA.

[†] Professor, Department of Aeronautical and Astronautical Engineering, 306 Talbot Laboratory, 104 South Wright Street; e-loth@uiuc.edu.

[‡] Aerospace Engineer.

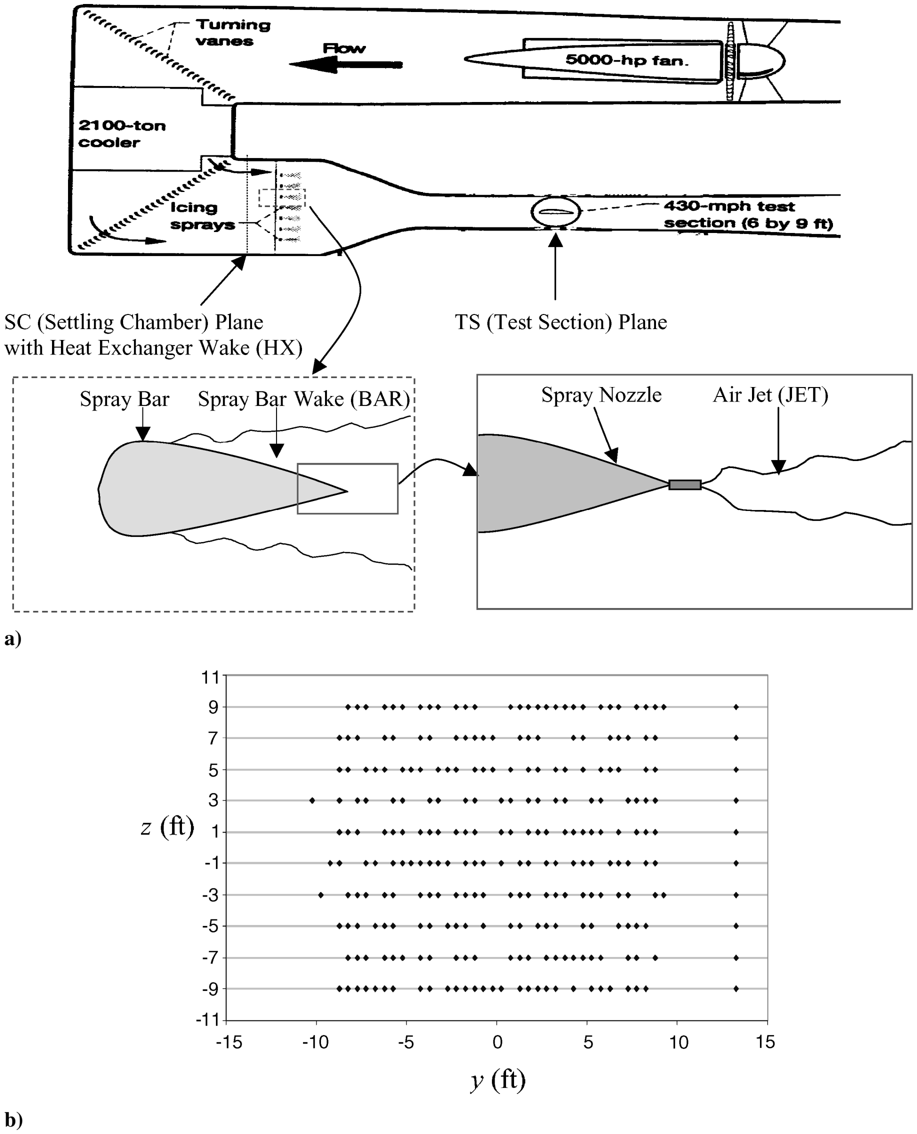

Fig. 1 Schematic of the a) IRT showing turbulent features including heat exchanger, spray bar, and jet flows and b) ——, bars and ♦, nozzles.

at the two stations[6] (settling chamber and test section) in terms of flow uniformity and a substantially decreased turbulence and flow angularity in the test section. In addition, there was an improved heat exchanger outflow characterization; specifically this included measurements of mean velocity, turbulence levels, and the power spectrum.

Such aerodynamic properties can play a critical role in the droplet dispersion and, thus, in the icing cloud uniformity. This is demonstrated in Fig. 2, which shows a sample droplet distribution in the test section plane for two cases, one where no turbulent diffusion is modeled and one where the turbulence diffusion was modeled based on Ref. 2. It can be seen that when the fluctuating velocities components, that is, turbulence, is set to zero, the particles move on the streamline to single points in the test section (Fig. 2a). However, when the turbulence is taken into account, the particles are dispersed according to the intensity of the turbulence and result into a much more uniform cloud formation in the test section, as seen in Fig. 2b. Thus, it is important to get an accurate prediction of the turbulence for an accurate prediction of droplet trajectories. As such, the objective of the present investigation is to develop a robust and accurate methodology for predicting the airflow for the updated IRT configuration and in particular the turbulence distribution from the spray bars to the test section. Future studies will investigate droplet trajectory calculations in hopes of eventually establishing a computational tool to allow NASA John H. Glenn Research Center engineers to predict accurately icing cloud quality, as well as droplet impingement, for a variety of tunnel and model conditions.

Numerical Methods

WIND Code

The computations herein solve for the steady-state compressible turbulent flow distributions using WIND 3.0 flow solver,[7] which contains a number of physical models and different algorithms. The turbulence model used is the shear stress transport (SST) k–Ω model. This model was used because it is known to predict turbulence reasonably for free-shear flows and boundary layers. The latter is important for the present simulations, which include the flow around an individual spray bar. Note that Hancir and Loth[2] used the k–ε model because they did not attempt to simulate flow around an individual spray bars and, thus, did not attempt to model any boundary-layer flows. Inflow conditions for the present simulations (specified for various domains) consisted of a nonuniform distribution of inflow velocity and turbulent kinetic energy k, with a uniform distribution of the temperature, pressure, and specific dissipation Ω. The FPRO utility of WIND was used to specify these inhomogeneous flow properties at the inflow plane. The outflow conditions consisted of a backpressure specification, which was set to obtain the correct cross-sectional test section velocity. As will be discussed, the wind-tunnel walls were assumed to be adiabatic and inviscid, such that the normal components of velocity were defined to be zero.

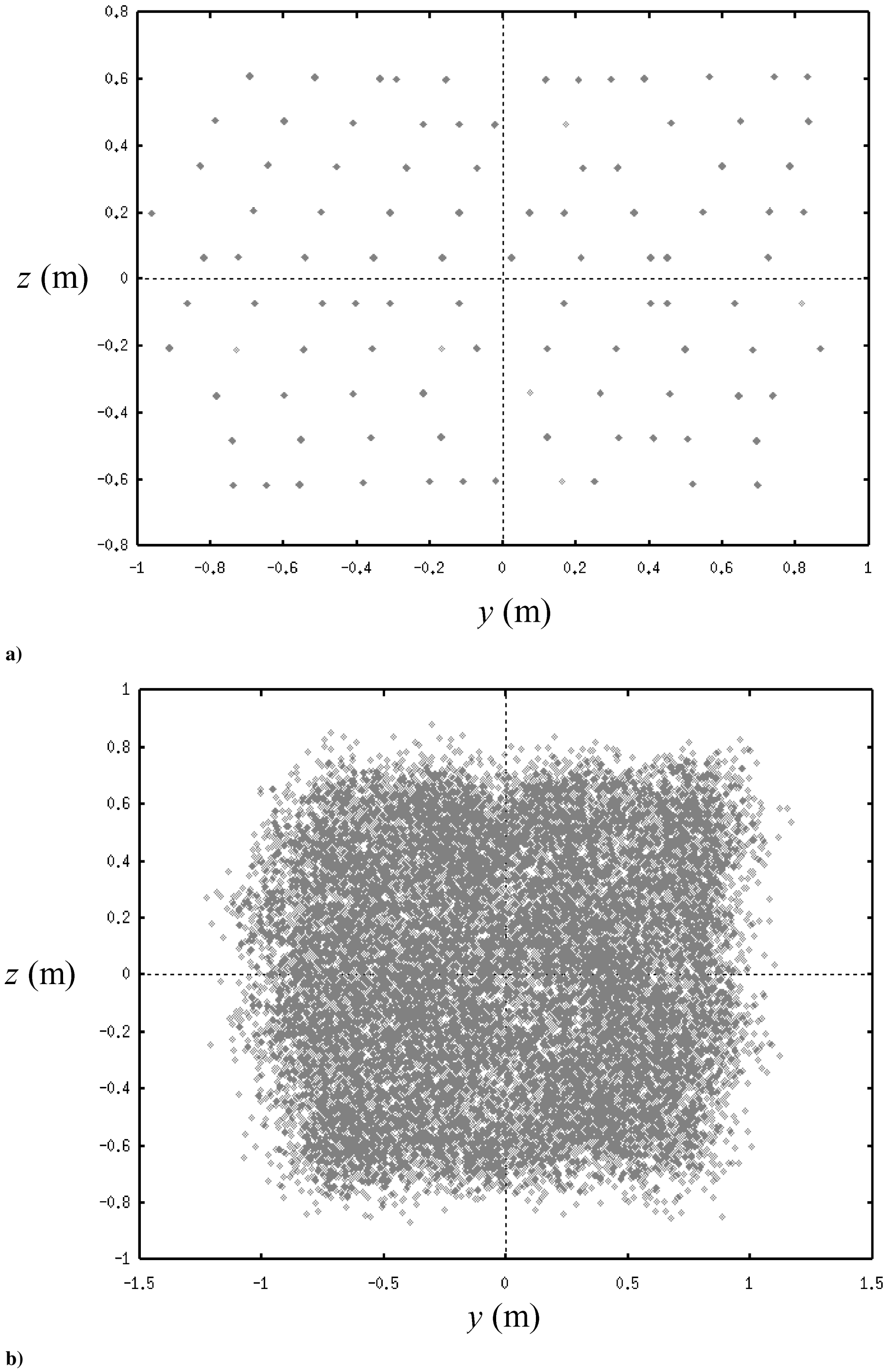

Fig. 2 Droplet distribution in the test section a) without turbulence and b) with turbulence (from Hancir and Loth[2]).

The steady-state solution is executed iteratively on the computational mesh using local time stepping where the flow equations are evaluated using second-order-accurate finite difference techniques. The partial differential equations are modeled in their conservative form, where the explicit terms are computed using a Roe upwind secondorder operator. The implicit terms are computed using a full block operator in the viscous directions and the scalar (diagonalized) matrix solver in the inviscid directions. All of the solutions were converged and reached steady state.

Wake Validation

A study was first completed to validate the code's ability to predict the turbulence decay in homogeneous wake flow based on the experiments of Snyder and Lumley.[8] This study measured the decay of turbulent kinetic energy of a grid-generated wake flow in a uniform square duct. Because the velocity components in the center region of the duct were negligible in the vertical and transverse directions, these were both set to zero in the WIND simulations. The mean axial velocity u was initialized to its experimental inflow value, and the computation was converged to a steady-state value to compare with the experimental results.

Snyder and Lumley's results[8] indicated that the decay of turbulent kinetic energy for their experiments is approximately given by

$$k = 1.5\bar{u}^2\left[\frac{1}{42.4(x/m - 16)} + \frac{2}{39.4(x/m - 12)}\right] \tag{1}$$

where x is the axial distance and m is the grid spacing in the axial direction. The present predictions (Fig. 3) show that the SST

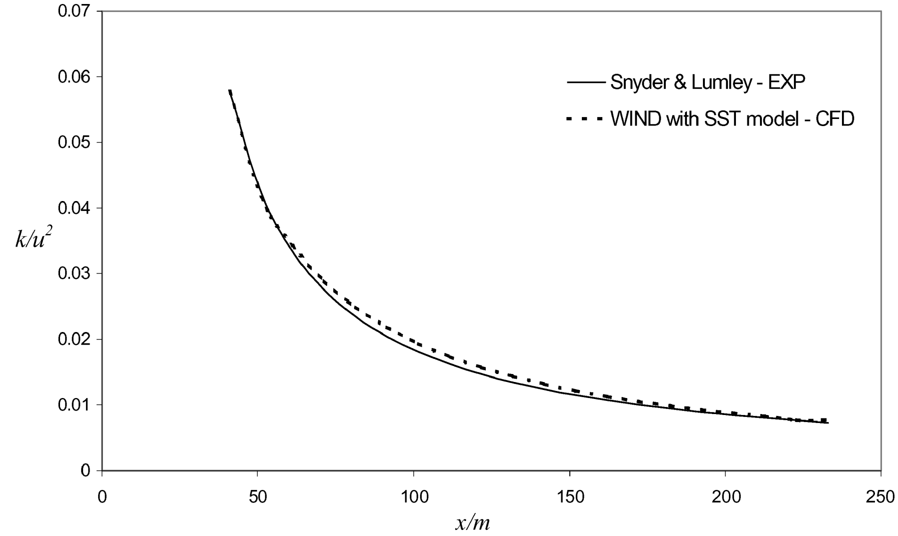

Fig. 3 Turbulent kinetic energy vs axial distance for WIND predictions evaluated against experimental data of Snyder and Lumley.[8]

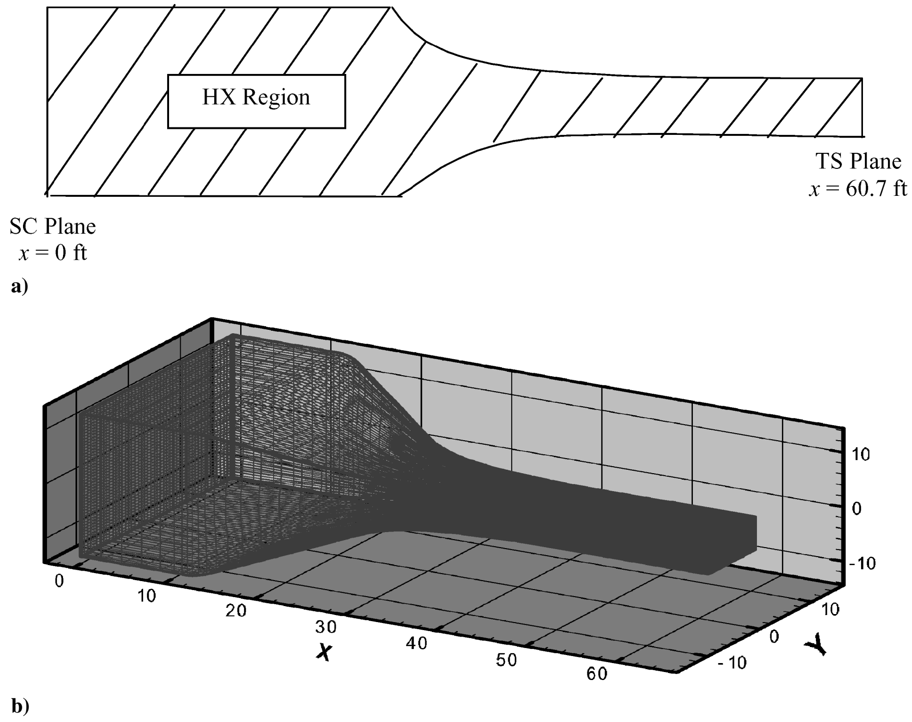

Fig. 4 HX computational domain showing; a) streamwise cut and b) computational grid.

WIND simulation reasonably matches the preceding empirical fit to the experimental results. Thus, the turbulence model approach was deemed reasonable for predicting the wake flows of the IRT.

IRT Relevant Turbulent Features

There are many factors that contribute to the evolution of the turbulence between the settling chamber and the test section. These factors can include the wake flow caused by the presence of the heat exchanger (HX), the wake flow caused by the presence of spray bars (BARS), the air jet flow emanating from their individual spray nozzle locations (JETS), and the boundary-layer flow caused by the presence of the tunnel walls. Previous studies by Hancir and Loth[2] showed that the tunnel wall boundary layers do not have a significant effect on the droplet trajectories, and, hence, this aspect was excluded from the present analysis. A schematic showing example features of the three remaining aspects is shown in Fig. 1a with the features denoted by HX, BAR, and JET.

To judge the importance of these features on the test-section turbulence, tunnel airflows with various combinations of these turbulent features were simulated independently. First, only the effect of the HX was taken into account (the HX flow description). Second, the effect of the wake from all of the spray bars was combined with the HX flow, resulting in the HX/BARS flow. Finally, an HX/BARS/JETS flow simulation was completed which further took into account all of the spray nozzle air jets.

Modeling the Wake of the HX

Methodology

The IRT was three dimensionally modeled from the settling chamber to the test section to obtain the test section aerodynamics as a function of the HX turbulence and velocity. Experimentally available inflow conditions approximately 5 ft upstream of the spray bars were used for the computations. Therefore, this measurement location was decided to be the start ($x = 0$ ft) of the HX computational domain (Fig. 4a), which spanned until the downstream test section location, where additional measurements were taken ($x = 60.7$ ft). At this test section location, experimental data were obtained by Gonsalez[6] and Arrington for the time-averaged streamwise velocity

u and mean transverse velocity v in the settling chamber, $x = 0$ ft, on both horizontal and vertical traverses. These were obtained at three horizontal traverses at z equal to 76, 156, and 234-in. (measured from floor) for several y positions and also obtained at three vertical traverses at y equal to 88, 196, and 263-in. (measured from inner wall) for several z positions. The measurements allowed for specification of the horizontal velocity angularity only because the time-averaged vertical velocity w was not measured and is, therefore, assumed herein to be negligible, that is, $w = 0$ at $x = 0$. In addition, u'_{rms} and v'_{rms} were measured and, thus, were converted into turbulent kinetic energy k by assuming $w'_{\mathrm{rms}} = v'_{\mathrm{rms}}$ (reasonable for wake flows[7]). Therefore, at start of the computational domain, $x = 0$,

$$k = 0.5\left(u'^2_{\mathrm{rms}} + 2v'^2_{\mathrm{rms}}\right) \tag{2}$$

$$V^2 = u^2 + v^2 \tag{3}$$

where V is the time-averaged total velocity magnitude.

The computational grid for HX (Fig. 4b) has $N_x = 50$, $N_y = 49$, and $N_z = 49$, where N_x, N_y, and N_z correspond to the number of grid points in axial x, transverse y, and vertical z directions, respectively, and were obtained based on a grid-convergence study. Tecplot was then used to interpolate and extrapolate the experimental data for a test section speed of 350 mph onto the computational inflow grid. The value of u and u'_{rms} on the walls was found by linear extrapolation (because wall boundary layers are neglected), and here v and v'_{rms} on the vertical walls were set to be zero consistent with inviscid wall boundary-layer conditions. Figure 5 shows the resulting interpolated axial velocity and turbulence vs the corresponding experimental data for a sample intermediate horizontal traverse. Note that, although some experimental scatter is superimposed on the velocity variations, the Tecplot interpolations do a good job of following the physical trends, especially with respect to the turbulence, where the sinusoidal variations of k in the experimental data are reproduced in the interpolated curve. These variations for k can be attributed to the spacing of the turning vanes upstream of the settling chamber plane (Fig. 1a).

The inflow turbulent dissipation ε was calculated using the power spectrum technique of Snyder and Lumley[8] and discussed as follows. When the hot-wire data (Gonsalez, J. C., personal communication, 2001) were used as input, LABVIEW provided the power spectrum for both u and v in the settling chamber and an empirical curve was then fit to this power spectrum data, for example, Fig. 6 shows the energy spectrum for the vertical velocity. The equation of the empirical curve was compared with the following theoretical equation to solve for the value of dissipation ε:

$$E(k) = \alpha \times \varepsilon^{\frac{2}{3}} \times k^{\frac{-5}{3}} \times \exp\left[-\left(\tfrac{3}{2}\right) \times \alpha \times (k \times \eta)^{\frac{4}{3}}\right] \tag{4}$$

$$\eta = (\nu^3/\varepsilon)^{\frac{1}{4}} \tag{5}$$

where α is equal to 1.7.

Because the test section experimental data were available at the test section mean velocity of 175 mph (Ref. 9), the interpolated data obtained in the settling chamber for the test section velocity of 350 mph (510 ft/s) were scaled to obtain the settling chamber data corresponding to test section velocity of 175 mph (255 ft/s). The axial, vertical, and transverse velocity were scaled by a factor of two (the ratio of the two test section velocities, 350/175). Because the turbulent kinetic energy k is proportional to square of the velocity, it was scaled by four. When the turbulent length scale was assumed to be constant, the dissipation was scaled by the velocity ratio cubed, that is, eight. The average of the resulting V and k over the inflow plane, as well as the uniform dissipation, is shown in the first column of Table 1.

Finally, the HX back pressure was fixed at the outflow (test section exit) to achieve a test section speed of 175 mph to agree with the measured speed for which test section aerodynamic data was available.

Results

Figures 7a and 7b shows the streamwise and cross-sectional axial velocity distribution for the HX solution. In Fig. 7a, the axial

Table 1 Average flow properties for HX for jets-off for test section speed of 175 mph

Flow property	Settling chamber, $x = 0$	Experimental results, $x = 50$ ft	HX flow solution, $x = 50$ ft
V_{av}, ft/s	19.4	255	257
k_{av}, ft^2/s^2	0.53	1.99	1.18
ε, ft^2/s^3	0.194	——	——

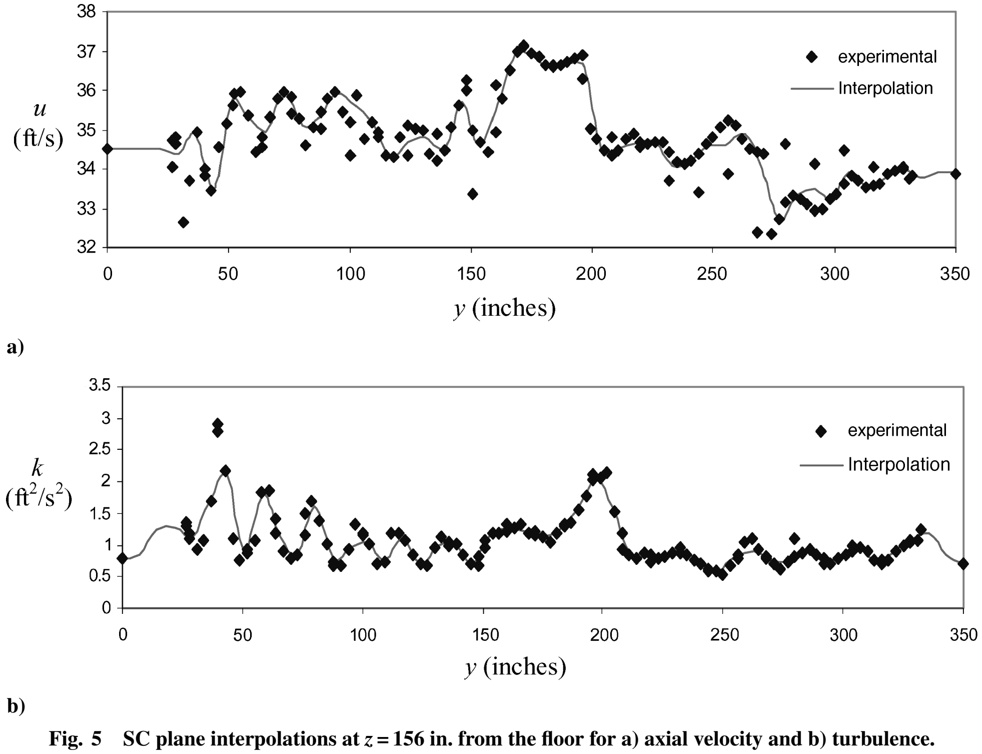

Fig. 5 SC plane interpolations at $z = 156$ in. from the floor for a) axial velocity and b) turbulence.

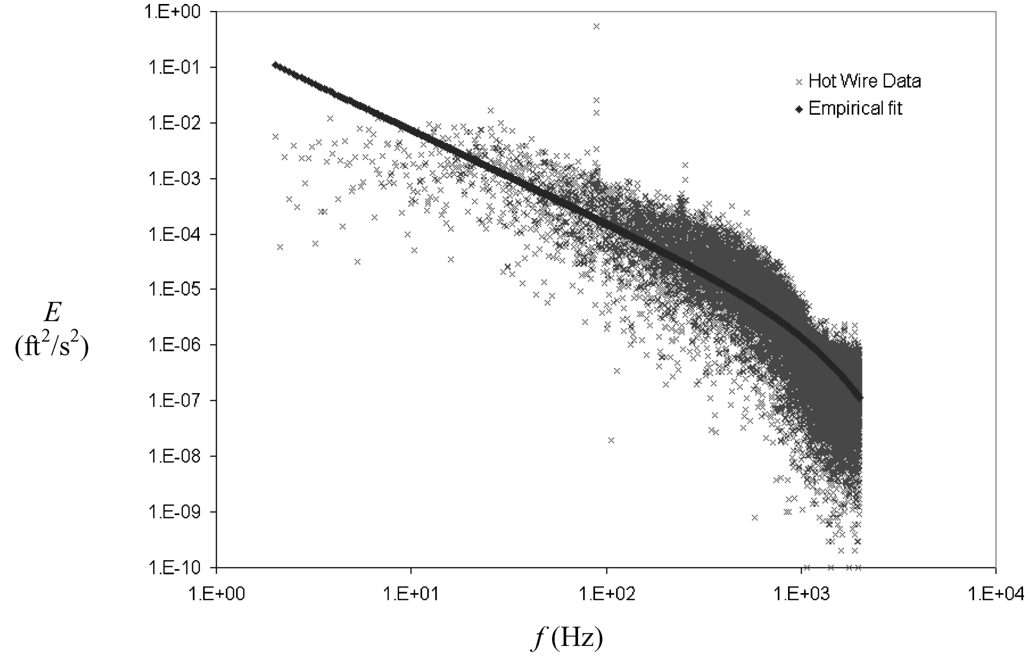

Fig. 6 Power spectrum for the vertical component of velocity from measurements by Gonsalez (personal communication, 2001) as compared to the theoretical curve.

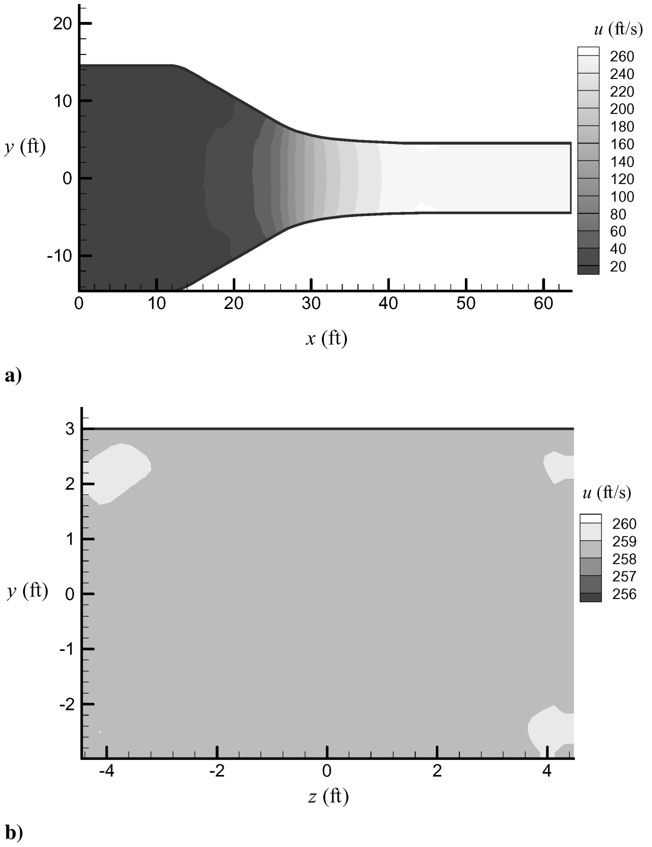

Fig. 7 HX axial velocity contours in a) x–y plane and b) test section plane.

velocity continuously increases from the settling chamber until the test section and then is approximately constant in the test section. The latter aspect is shown more clearly with the cross-section plot of the axial velocity contours (Fig. 7b), where only minor deviations are noted in the corner.

Figure 8a shows the predicted turbulence distribution in the test section. Notice that the highest values of turbulence are found in the corners. This is result of the high-velocity gradients in the corners near the inflow, which gave rise to an increase in μ_t and, thus, in k as the flow evolved downstream. Figure 8b shows the predictions and measurements at two probe transverse stations as indicated by dashed lines. A consistent underprediction of k is found and can be attributed to neglecting the wake produced by spray bars downstream of settling chamber. This is because the spray bars are expected to have significant wake because they have a shape of an airfoil but with a very large maximum thickness (t/c of 32%) such that substantial turbulent shedding can be expected.

To get an overall evaluation, the results of HX flow averaged over the cross-sectional plane of the test section are summarized in Table 1 along with the measured values. Note that the average test section velocity V_{avg} is correctly predicted. The cross-sectional averaged k in the test section, k_{avg}, was higher than given at the inflow plane, but substantially lower than that measured at the test section (for the jets-off case), thus, confirming the trend noted in Fig. 8b. Thus, to get a more accurate prediction of test section turbulence with jets-off, a new simulation was required that incorporated the spray bar wakes.

Modeling Flow Around a Single Spray Bar Wake

Methodology

Because the flow downstream of the spray bars is approximately the same for all of the spray bars, it was sought first to simulate flow around a single spray bar (for later combination with the HX flow). The inflow conditions for this single spray bar domain were the cross-section-averaged properties in the settling chamber upstream of the spray bars (Table 1). Because the spray bars were largely two dimensional (aside from a center strut), a two-dimensional computational domain was used (Fig. 9), which spanned from the measured settling chamber (SC) plane, $x = 0$ ft, until the beginning of the contraction section of the tunnel, $x = 12.9$ ft. A backpressure was specified at the outflow such that there was negligible flow acceleration from the inflow to the outflow to be consistent with the negligible mean acceleration seen for the HX flow over this range. Slip boundary conditions were specified halfway between neighboring spray bars to represent a condition of symmetry for spray bars above and below this domain. (The vertical centerline distance between two spray bars is 2 ft). The surface of the spray bar was specified as a viscous surface (no-slip conditions) because the resulting boundary layers are important to the downstream wake fidelity.

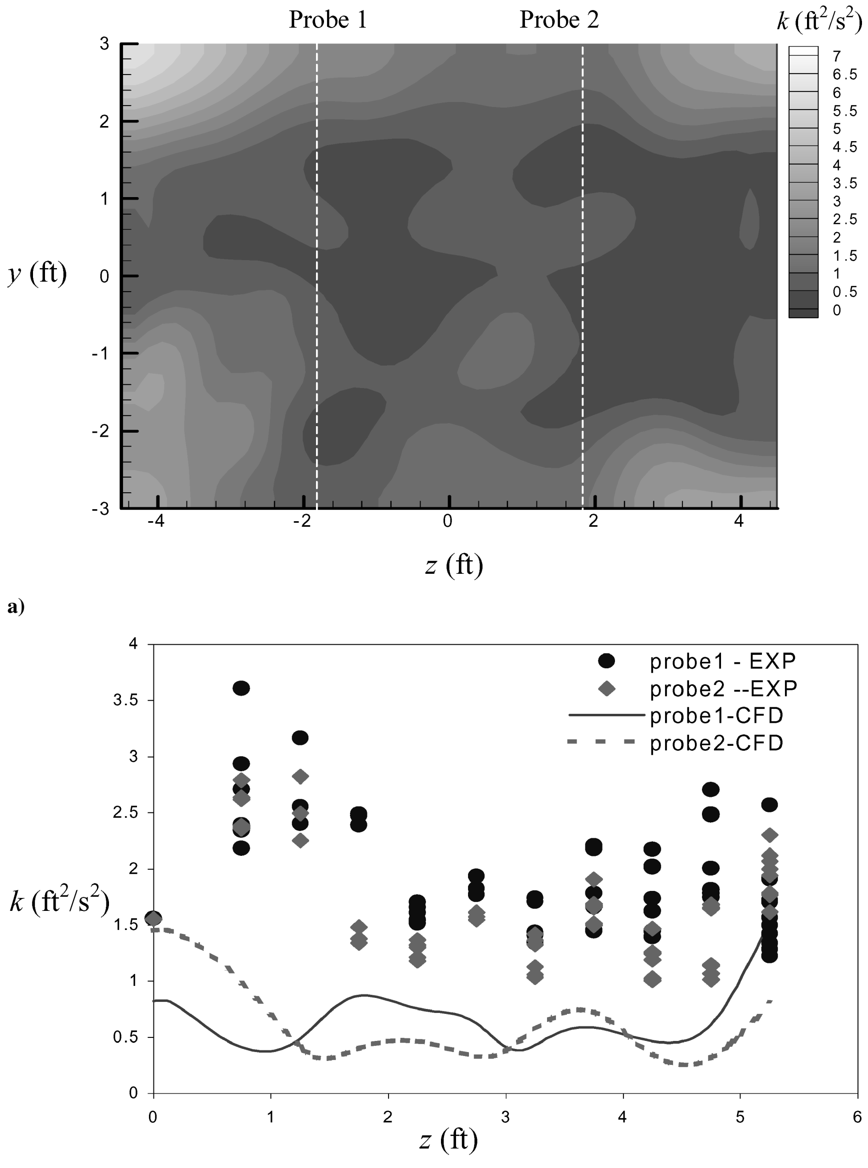

Fig. 8 Turbulence at test section a) contour plot and b) comparison with experimental data.

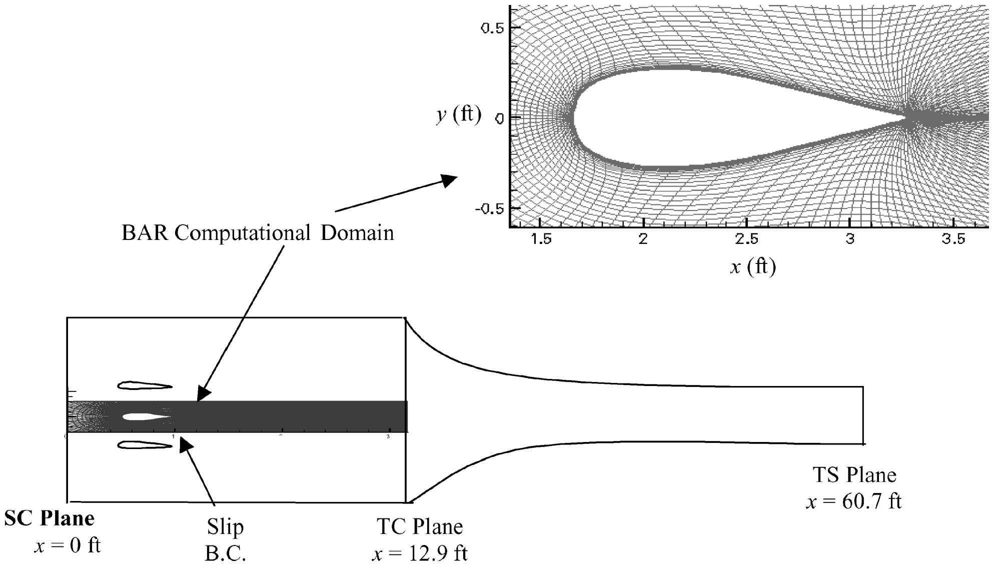

Fig. 9 Spray BAR computational domain with close-up of computational grid around spray bar.

The computational grid (Fig. 9) generated around the spray bar is a C grid with the first normal grid point at y^+ of about 1. This grid was generated using the GRAPE software code, with a vertical extent consistent with the spray bars' spacing. A grid-convergence study was completed to make sure the solution was independent of the spatial resolution used. Based on this, the grid used for present simulations has 21,000 grid cells with 350 points in streamwise direction and 60 points in normal direction.

Results

The results of the flow around a single spray bar are shown in Fig. 10. The axial velocity (Fig. 10a) decreases along the spray bar centerline and is zero at the spray bar leading edge, and above the boundary layer it increases till the maximum thickness (at $x \sim 2$ ft), and then it decreases again until the spray bar trailing edge. A wide velocity deficit can be noticed in the spray bar wake, which includes a small separated flow region. As a result, the turbulence in the spray bar wake region is much higher than in the freestream region (Fig. 10b). A comparison of the spatially averaged flow properties at the outflow of the BAR domain, that is, at $x = 12.9$ ft, is given in Table 2, along with the HX average flow properties at this same axial location. The BAR results clearly indicate that spray bars do not lead to significant flow acceleration, that is, V_{av} is approximately constant. However, the amount of turbulence in the flow substantially increases from $x = 0$ to $x = 12.9$ ft and is more than five times larger than the flow with out the spray bar, that is, the HX flow. This indicates that all of the spray bars should be included in the wind-tunnel simulation to better describe the turbulence.

Table 2 Average flow properties before contraction, jets-off

Flow property	At BAR inflow, $x = 0$ ft	At BAR outflow, $x = 12.9$ ft	HX flow solution, $x = 12.9$ ft
V_{av}, ft/s	19.7	21.5	20.1
k_{av}, ft^2/s^2	0.53	5.19	0.91

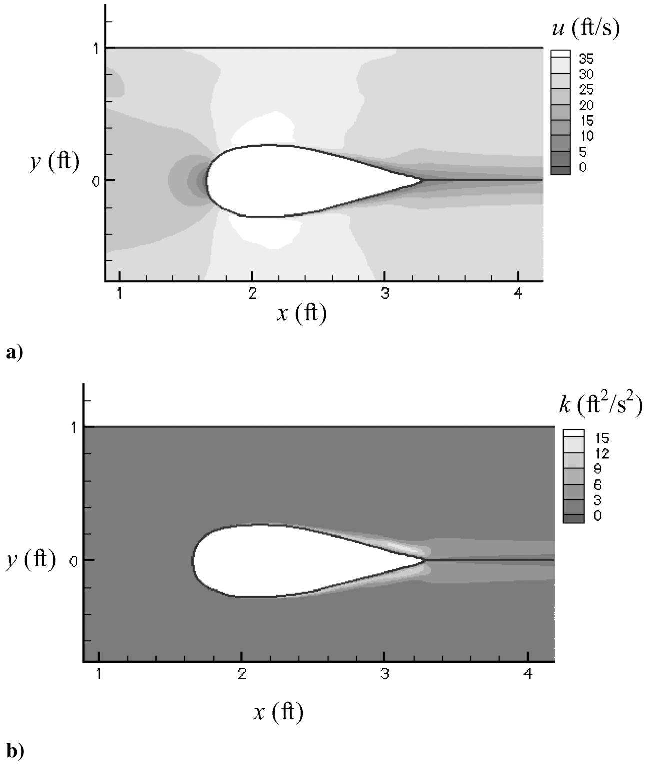

Fig. 10 Spray BAR contours of a) axial velocity (feet per second) and b) turbulence (square foot per second squared).

Modeling Wakes of HX/BARS

Methodology

As noted earlier, it is desired to incorporate the mean turbulent flow features associated with both the spray bar wake details and the wind-tunnel three-dimensional geometry. However, it is not practical to construct a single computational grid, which simultaneously resolves the thin boundary layers of all of the spray bars while also retaining the full geometry of the wind tunnel (60.7 ft long from the settling chamber until the test section). Thus, to accomplish such an integrated wind-tunnel simulation, the aspects of the wakes of the HX/BARS required some integration, which was accomplished herein by an approximate linear combination. The schematic for this combination is shown in Fig. 11a and is described in the following. At its inflow plane, $x = 4.3$ ft, the wake of the 10 spray bars and the HX flow were combined to create an HX + BARS inflow plane using a combination of the $x = 4.3$ ft results of the HX flow and that of the individual spray bar wake (BAR) applied downstream of each of the 10 spray bars locations. In particular, a min/max approximation was used for the HX + BARS plane ($x = 3.8$–4.3 ft), where each flow variable ϕ at any given y, z location was set to the maximum of the local BAR value and the overall HX flow value, except for the axial velocity, where the minimum was specified to allow for the velocity deficit of the spray bar wake. In other words,

$$\phi_{\mathrm{HX+BARS}} = \max(\phi_{\mathrm{HX}}, \phi_{\mathrm{BAR}}) \tag{6}$$

$$u = \min(u_{\mathrm{HX}}, u_{\mathrm{BARS}}) \tag{7}$$

where ϕ represents ρ, v, w, k, and Ω. This combination ensures that the flow is characterized by the dominating extremes given by either of the two solutions. Thus, the regions where flow angularity, turbulent kinetic energy, and Ω are larger for the BAR flow are assumed to take on only the BAR wake features. In particular, this min/max technique can only be reasonable for the condition where these flow features (angularity, turbulence, and momentum deficit) are much greater for the BAR flow than for the HX flow, e.g., $k_{\mathrm{BAR}} \gg k_{\mathrm{HX}}$, such that the small perturbation from the HX flow is approximately negligible. Note that this algebraic combination is not formally consistent

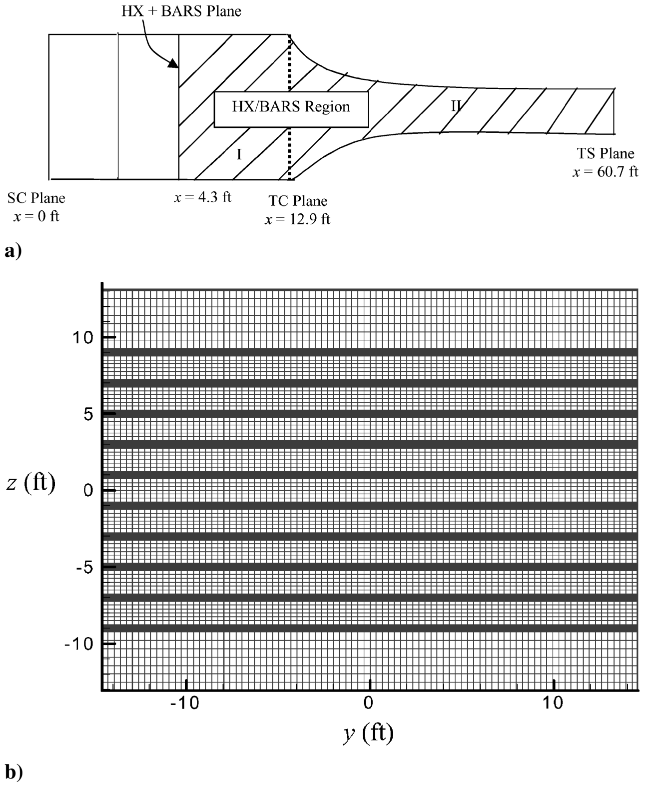

Fig. 11 HX/BARS flow showing a) computational domain and b) grid at inflow plane at $x = 4.3$ ft (where variables are based on HX + BARS).

with the partial differential equations, which govern the conservation of mass and momentum, and thus, this technique is unsuitable for combining flows in general. However, because the combinations are conducted for specific conditions where one flow contains turbulence or a velocity deficit that dominates that of the other flow, it can be considered similar to a small perturbation technique. Thus, if one flow dominates in terms of turbulence, the variations between this algebraic combination and a properly integrated flowfield can be expected to be small (an example of which will be shown later).

In the region of the BAR wake centerline, this condition is realized because the HX flow is a small perturbation for the present conditions, for example, $k_{\mathrm{HX}} = (0.05)\, k_{\mathrm{BAR}}$ at HX + BARS plane. Recall that such an approximation is needed because the ideal simultaneous numerical resolution of the three-dimensional wind-tunnel flow and that the details of the BAR boundary layers are not practical due to the immense computational resolution that it would require.

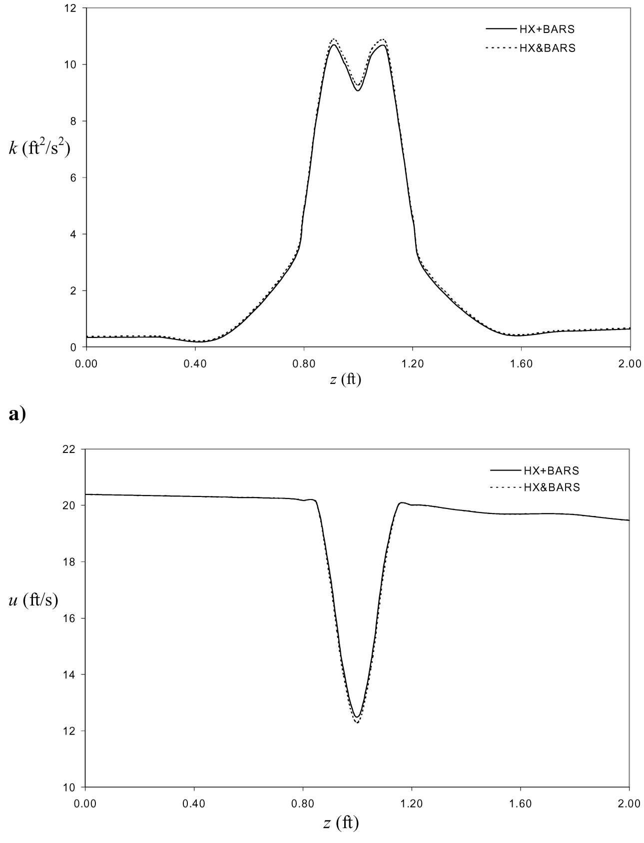

Fig. 12 Comparison of properties between HX + BARS and HX and BARS at the axial location 4.3 ft for flow about the fifth spray bar.

To evaluate the application of min/max technique for the HX+BARS flow, the flow downstream of the fifth spray bar was also computed with a proper simulation of the flow, that is, using the spatially varying heat exchanger flowfield as an inflow and then simulating the flow around the spray bar. This fully integrated result is referred to as the HX and BAR solution. Figure 12 shows the velocity and turbulence comparison at $x = 4.3$ ft between the HX and BAR solution (with no combination assumptions) and the HX + BARS solution (with linear combination assumed). The maximum differences between the two results were found to be 2% for the turbulence and 1% for mean axial velocity. Thus, in the particular case, it is reasonable to consider a single BAR flow with averaged HX inflow conditions and then to linearly combine this result with the spatially varying HX flow at a downstream plane to describe the flow downstream of all of the spray bars.

The inflow distribution obtained through this min/max combination of solutions is shown in Fig. 13 at the HX/BARS inflow plane for u and k. As expected, the effect on the axial velocity is small because the wake deficits were small compared to the mean flow at this location, $x = 4.3$ ft. However, the spray bars cause a significant increase in the turbulence, due to their wake stemming from a high t/c ratio of 32%.

The grid at the inflow plane for the HX/BARS is shown in Fig. 11b, where one can notice a high resolution of the regions just downstream of the 10 spray boundaries, required to resolve properly the spray bar wakes. To minimize the computational time, the HX/BARS computational domain consists of two zones, as shown in Fig. 11a. The zone 1 computational grid (from $x = 4.31$ to $x = 12.9$ ft) had $N_x = 6$, $N_y = 89$, and $N_z = 169$, whereas the zone 2 grid (from $x = 12.9$ to $x = 60.7$ ft) had $N_x = 40$, $N_y = 69$, and $N_z = 169$.

Computations were first carried out for zone 1 with the backpressure specified for negligible flow acceleration (consistent with the constant cross section and no tunnel wall boundary layers). A grid-convergence study for this zone was completed by keeping the number of points in the axial direction, N_x, fixed and varying in the transverse direction, N_y. Figure 14 shows a sample of the grid-resolution results for variation of N_y from 49 to 109 for the preceding N_x and N_z resolution, where it is seen that an N_y of 89 was sufficient. Additional resolution tests indicated that the preceding N_x and N_z were also sufficient for grid independence. The outflow of zone 1 was used as the inflow to zone 2, where the backpressure was again fixed at the outflow to achieve a test section speed of 175 mph to agree with the measured test section speed.

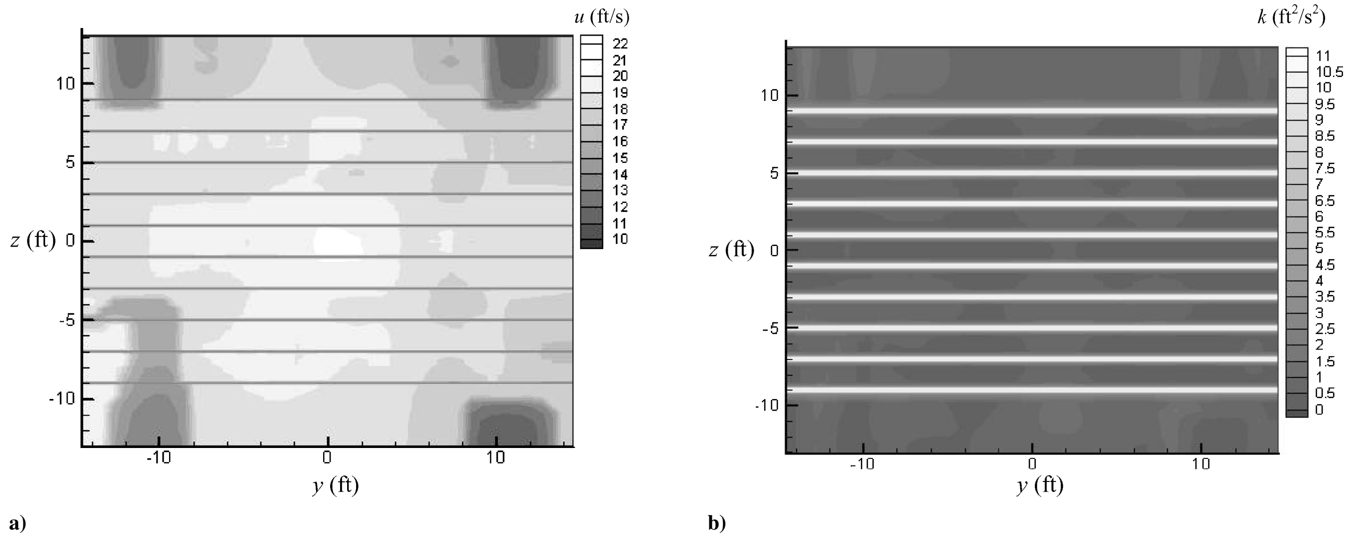

Fig. 13 HX/BARS inflow contours for a) axial velocity and b) turbulence.

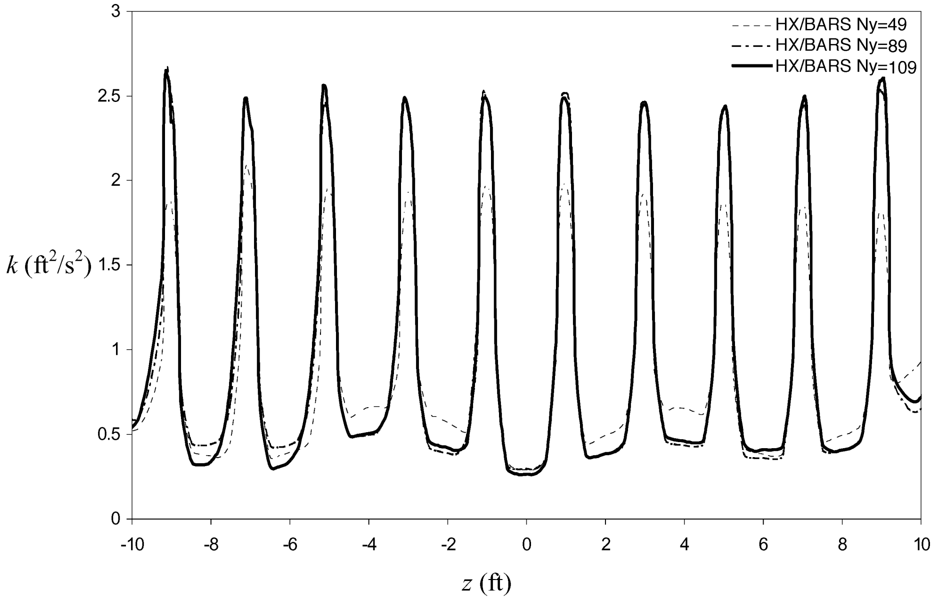

Fig. 14 Spanwise resolution effects ($Nx = 6$) on variation of zone 1 outflow turbulence at $x = 12.9$ ft and $y = 1.1$ ft.

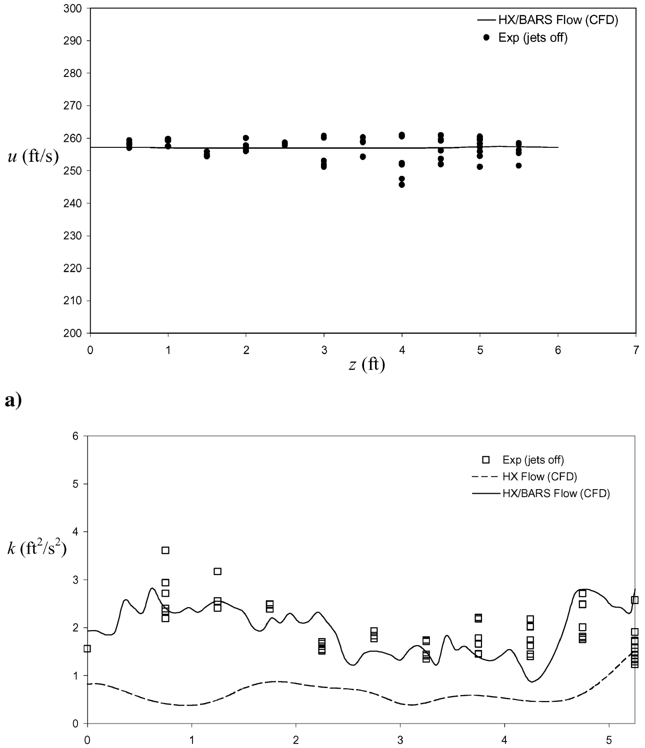

Fig. 15 Comparison of experimental data by Gonsalez et al.[9] for probe 1 (2.6 ft from inside vertical wall) with a) HX/BARS predictions for axial velocity in x–y plane and b) HX and HX/BARS flow turbulence in test section.

Results

Although not shown, the axial velocity variation in the test section for HX/BARS flow was found to be very similar to that for the HX flow (Fig. 7a). Specifically, the mean velocity was found to increase from the settling chamber until the test section and then is approximately constant in the test section. This latter aspect is shown in Fig. 15a, with the comparison of axial velocity predictions in the test section with the experimental data measured at $y = 2.6$ ft from the inner wall. The variation in the experimental data (from different test runs) was on the order of the variations such that no significant variation of u in the z direction was found. Thus, the predicted results, which indicated a nearly uniform velocity, are within the variations of the velocity measurements. Similarly, the cross-sectional averaged experimental axial velocity along the traversal, 257.2 ft/s, was close to the cross-sectional-averaged predicted value of 257.3 ft/s. Thus, the axial velocity was reasonably predicted again by taking spray bars into account (though the previous HX predictions also reasonably predicted the axial velocity).

Table 3 Test section properties for jets-off and jets-on (80 psig) for test section velocity of 175 mph

Flow property	Experimental results jets-off, $x = 50$ ft	HX/BARS jets-off, $x = 50$ ft	Experimental results jets-on, $x = 50$ ft	HX/BARS/JETS $x = 50$ ft
V_{av}, ft/s	255	257	255	258
k_{av}, ft^2/s^2	1.99	1.96	16.59	15.47

To note the impact on turbulence, the predictions were compared to measurements at the data traversal located at $y = 2.6$ ft from the inner wall of the test section plane (Fig. 15b). It was found that taking spray bars into account results in a significantly higher test section turbulence as compared to that for the HX flow. The HX/BARS flow predictions yield reasonable agreement with the experimental trends (Gonsalez, J. C. personal communication, 2001) at this transverse location. In particular, the predictions are within the variations of the turbulence measurements. For an overall comparison, Table 3 shows the cross-section spatially averaged u and k in the test section for the HX/BARS simulations as compared with the experimental conditions at all traverses. This indicates that taking the spray bars wake into account yields an accurate prediction of turbulence in the test section for the jets-off condition.

Modeling a Single Spray Nozzle Air Jet (JET)

Methodology

To study the flow of an individual air jet at air pressure of 80 and 20 psig, a three-dimensional Reynolds averaged Navier–Stockes (RANS) simulation was completed. The JET computational domain in the horizontal and vertical directions (Fig. 16a) spanned from the center of the nozzle orifice to halfway between the neighboring nozzle exits, that is, it spanned 0.25 ft horizontally and 1 ft vertically. For the inflow to JET, the jet flow was specified as uniform from the nozzle center until the nozzle radius of 0.0625 in. (consistent with the converging nozzle geometry) with a stagnation pressure equal to nozzle chamber air pressure (80 and 20 psig). The rest of the surrounding JET inflow region was initialized using the HX/BARS solution, that is, spray bar wake, at $x = 3.3$ ft (1 in. downstream of the trailing edge of the spray bar). Slip boundary conditions were specified on the vertical and horizontal planes of symmetry of the domain such that only one-fourth of the jet development was actually simulated. The computational domain in the axial direction spanned from nozzle location, $x = 3.3$, to a point, $x = 4.3$ ft, where an individual jet had spread significantly but did not yet substantially affect the edge velocities (so that jet merging had not yet occurred). The average axial velocity on the horizontal and vertical outside edges of the domain at the outflow was 1% higher than the HX flow at this location (whereas the centerline velocity was 314.2% higher).

The computational grid consisted of three zones to minimize the computational time. The computational grid is highly resolved in zone 1 to resolve the initial air jet development with eight grid points across the nozzle radius and an initial streamwise resolution equal to two nozzle diameters. The grid spacing increases in vertical direction on moving from zone 1 to zone 3 (Fig. 16b). In particular zone 1 included $N_x = 49$, $N_y = 39$, and $N_z = 41$; zone 2 included $N_x = 49$, $N_y = 39$, and $N_z = 24$; and zone 3 included $N_x = 49$, $N_y = 39$, and $N_z = 25$.

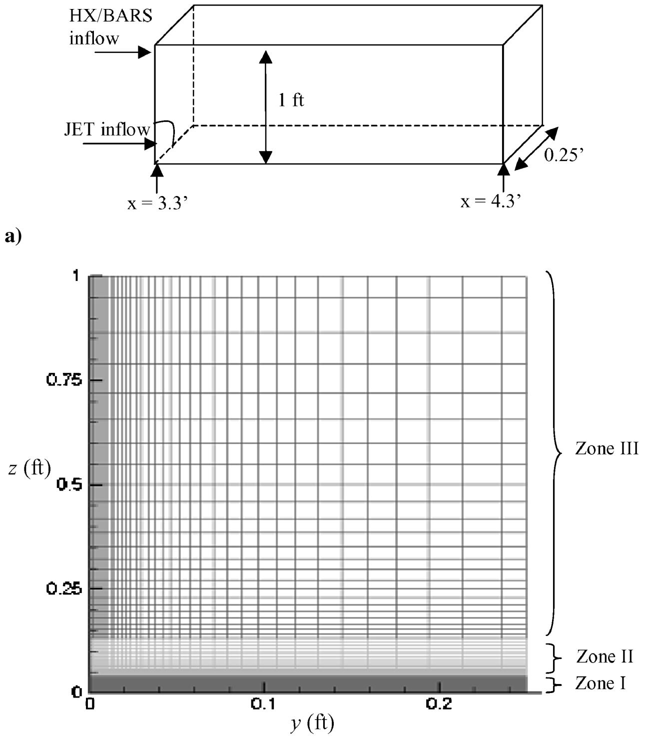

Fig. 16 JET domain showing a) computational domain and b) y–z grid at inflow plane ($x = 3.3$ ft).

Results

The Mach number distribution, with streamwise development and outflow contours are shown in Fig. 17a and 17b, respectively, for jet air pressure equal to 80 psig. Figure 17a shows that the jet width expands continuously from inflow (1/16 in. radius) to the outflow (~0.1 in. radius), but initially includes a high centerline speed before eventually decaying. (Outflow is entirely subsonic.) At the outflow plane (Fig. 17b), the results reveal the spray bar wake deficit along $z = 0$ but with a high velocity at the jet centerline ($y = 0$) equal to 87 ft/s. Far from the jet centerline, the results tended to the HX solution, for example, 18 ft/s at $z = 0.5$ ft and $y = 0.25$ ft. It was found that the JET outflow turbulence level at $x = 4.3$ ft is much higher than the average BAR or HX turbulence levels in the vicinity of the jet, but the magnitude decreased rapidly away from the jet. In particular, the peak turbulence was found at the jet centerline, for example, 8400 ft^2/s^2 at $z = 0$ and $y = 0$ ft, but tended toward the BAR result along the bar horizontal plane but away from the jet, for example, 10.5 ft^2/s^2 at $z = 0$ and $y = 0.25$ ft, and tended to the HX result away from both the bar and jet wake, for example, 0.8 ft^2/s^2 at $z = 0.5$ and $y = 0.25$ ft. Note that JET simulation was also done at jet air pressure of 20 psig.

Modeling Wakes of HX/BARS/JETS

Methodology

The effect of the air jets was combined with the HX and BAR results by defining a new computational domain (HX/BARS/JETS) as shown in Fig. 18a. The HX+BARS+JETS inflow plane for this domain combines the converged RANS solution of the HX+BARS flowfield with the JET results implemented at each nozzle location (Fig. 1b). This combination was obtained at each grid point by setting each flow variable ϕ to be the maximum of the JET flow variable and the HX + BARS values, that is,

$$\phi_{\mathrm{HX+BARS+JETS}} = \max(\phi_{\mathrm{HX+BARS}}, \phi_{\mathrm{JETS}}) \tag{8}$$

where ϕ represents ρ, u, v, w, k, and Ω.

This approximation is similar to that used for the HX/BARS inflow plane. Again this technique is not generally rigorous or appropriate, but it is expected to be reasonable because the axial velocity

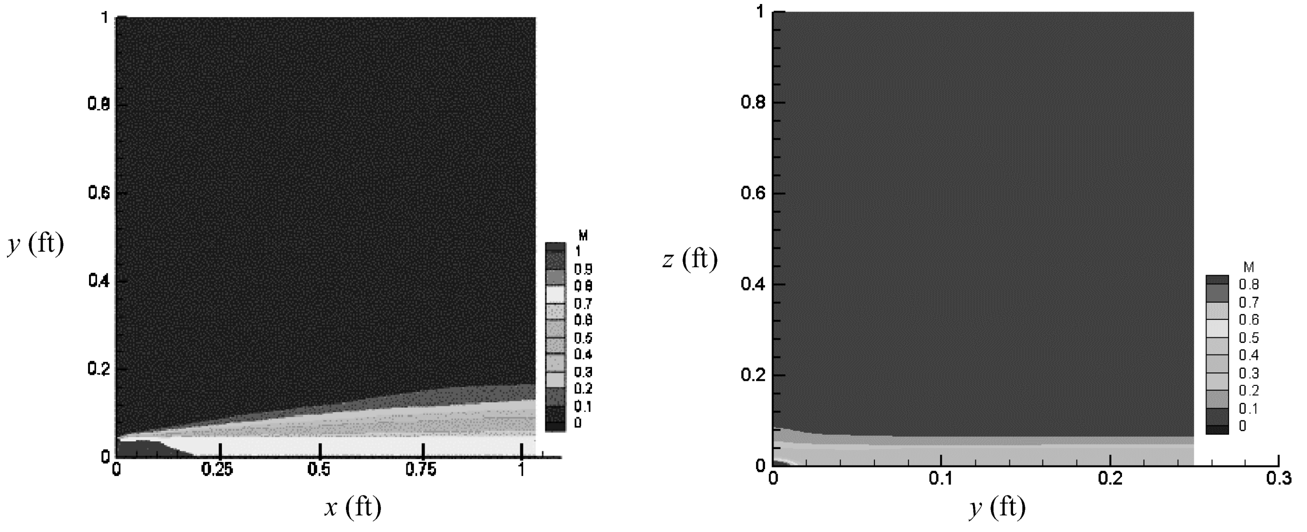

a) b)

Fig. 17 JET flow showing Mach contours at a) along the jet centerline in x–z plane and b) outflow y–z plane ($x = 4.3$ ft) for air jet pressure of 80 psig.

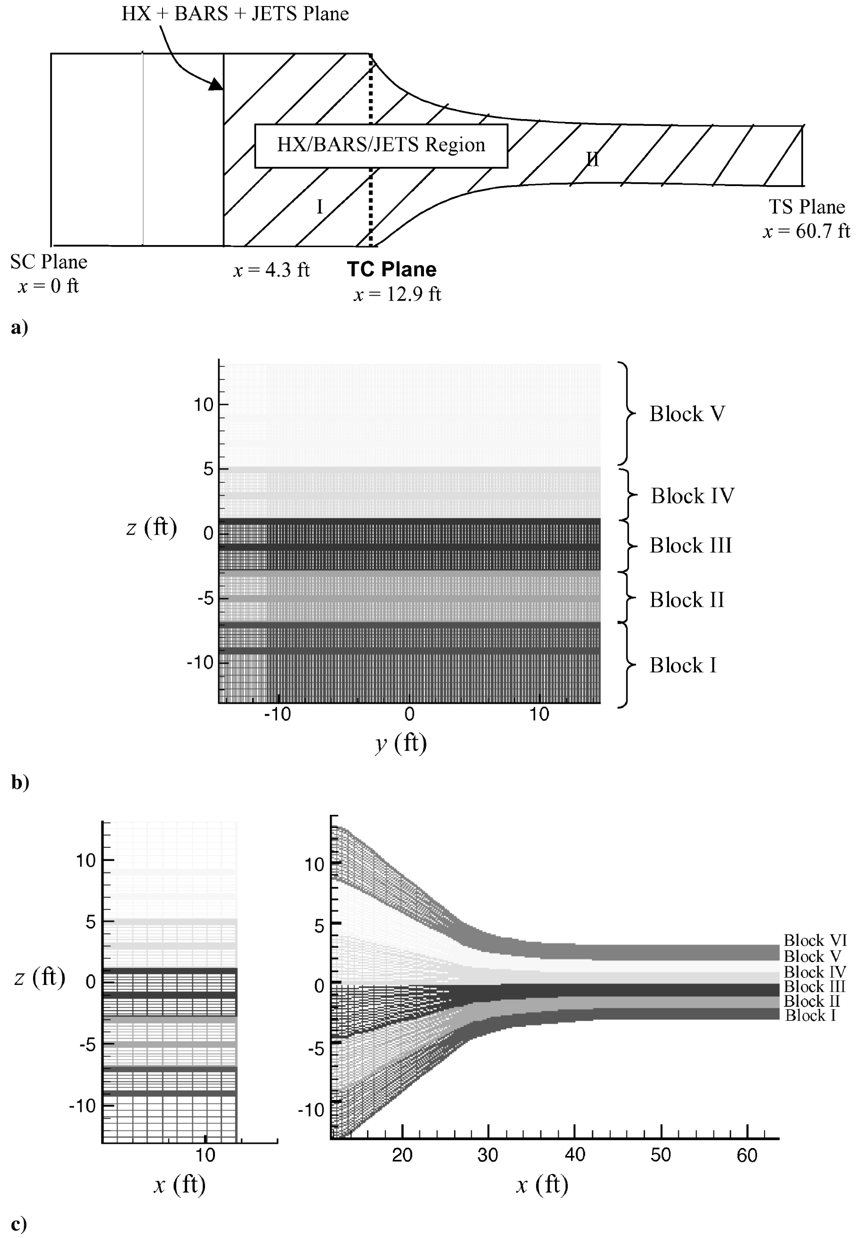

Fig. 18 HX/BARS/JETS flow a) computational domain, b) zone 1 grid at inflow, and c) zone 1 and 2 computational grid in x–z plane.

and the turbulence caused due to the air jets are much higher locally than that caused due to the heat exchanger and the spray bars (as already discussed). Thus, the axial velocity and the turbulence due to the heat exchanger and the spray bars can be considered as a small perturbation to the jet flow and may be neglected in the regions dominated by the air jets. Again, note that computationally resolving all of the jets (starting from the nozzle orifices) and the tunnel flow would require a prohibitively large number of data points, for example, over 20 million grid points if the present resolution for JET was employed throughout. The plane where these three simulations were combined (HX+BARS+JETS) is located where the individual jets began to merge, $x = 4.3$ ft, so that the assumption of an individual jet in a uniform coflow would be reasonable at this point. The HX+BARS+JETS inflow plane contours for air jet pressure of 80 psig are shown in Fig. 19, where the spray bars yield 10 weak wake deficits at this plane, whereas the jets lead to small but distinct peak velocities within the spray bar wakes. For the turbulence contours, the increase in k due to both the spray bars and the jets is more pronounced. The increase in velocity and turbulence due to jets with air pressure of 20 psig was found to be much less compared to 80 psig but higher compared to the HX and BAR velocity and turbulence.

To minimize the computational time, the computational domain for HX/BARS/JETS consists of two zones, as shown in Fig. 18a. Figure 18b shows the computational grid at the zone 1 inflow plane. The zone 1 computational grid has 642,000 points (necessary to ensure at least six grid points across all of the jet diameters at $x = 4.3$ ft). Zone 2 computational grid has six blocks and 633,000 points (Fig. 18c). Both of the computational zones were further divided into five blocks, so that each was solved using parallel processing. The backpressure was applied at the outflow to achieve a test section speed of 175 mph.

Results

Although not shown, the axial velocity was found to increase from the settling chamber to the test section and then was approximately constant in the test section, similar to the HX flow (Fig. 7a). Figure 20a shows a comparison of the axial velocity at the test section, $x = 50$ ft between the predictions and the experimental data traversals for $z = 3$ ft at $y = 2.6$, 4.5, and 6.4 ft. The predicted results were found to be within the variation of the experimental results taken for different runs (Gonsalez, J. C., personal communication, 2001). Note that Fig. 15a shows the axial velocity variation in the

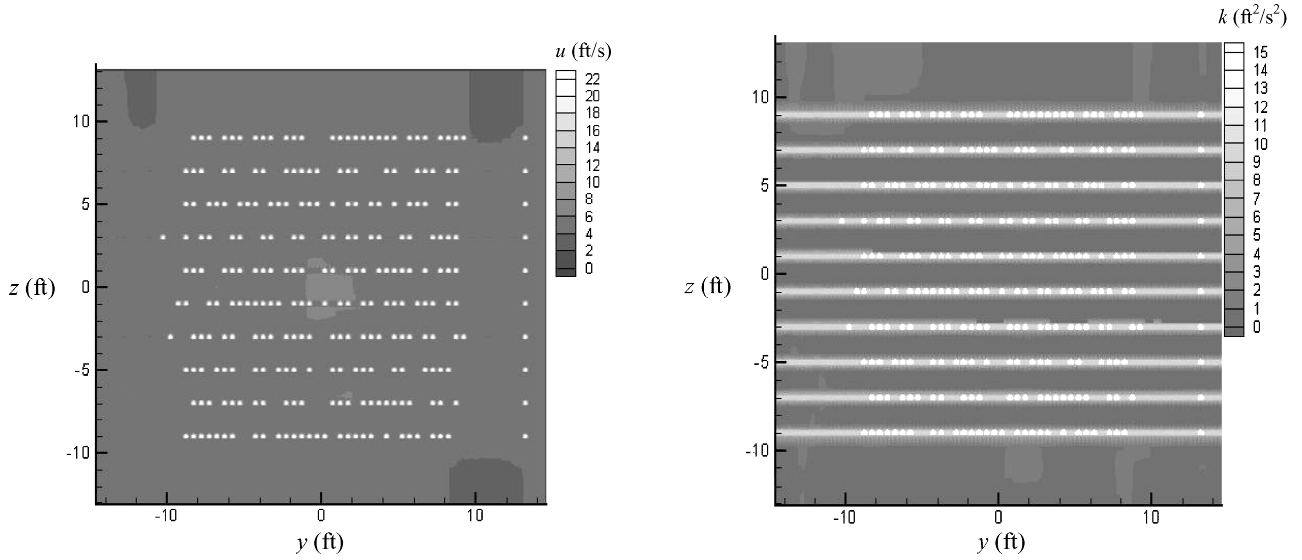

a)

b)

Fig. 19 HX/BARS/JETS inflow contours for a) axial velocity and b) turbulence.

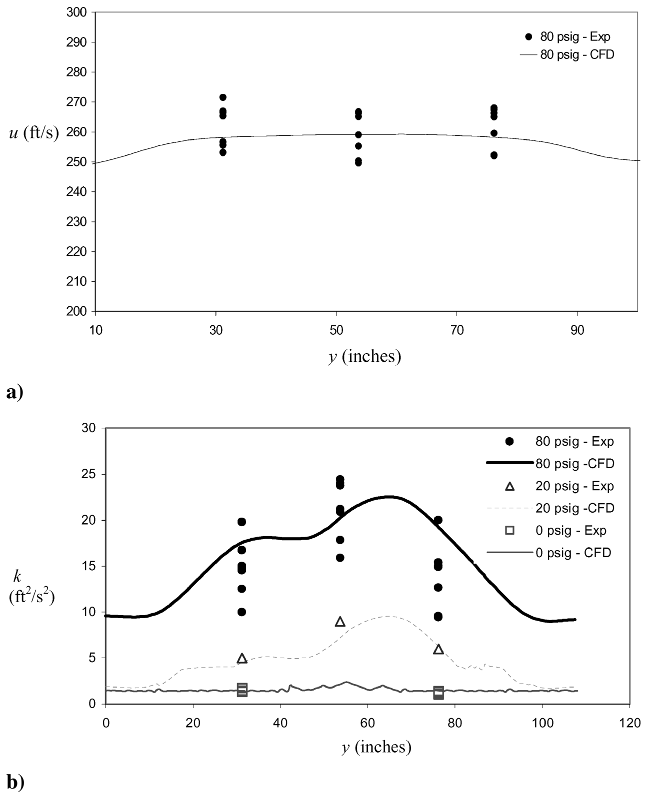

a)

b)

Fig. 20 Comparison of predictions with experimental data by Gonsalez (personal communication, 2001) for a) axial velocity with jets-on (80 psig) and b) turbulence in test section for jets-off (0 psig with HX/BARS) and jets-on (80 and 20 psig).

test section for the jets-off case (0 psig). Figure 20b shows the turbulence at the test section, $x = 50$ ft, for the jets-on and jets-off cases at a horizontal traverse. In comparison to the jets-off results, there is a significantly higher turbulence for both the experiments and the predictions. In addition, the inclusion of the air jets at 80 and 20 psig in the HX/BARS/JETS simulation yielded predictions that reasonably matched the experimental turbulence, both in terms of spatial trends and overall magnitudes. Note that the experimental data for turbulence at jet air pressure of 20 psig was obtained assuming isotropic turbulence which is $u' = v' = w'$, that is, v' and w' were taken to be equal to u' due to some inconsistent data for v'. Table 3 shows a comparison of spatially averaged velocity and turbulent kinetic energy in the test section for the experimental data and for the simulations ($z = 36$ in. and averaged for all y). For both jets-off and jets-on (80 psig), the predictions are found to provide a good estimate of mean test section velocity and turbulence level.

Conclusions

A numerical analysis of the airflow in the IRT was constructed with WIND using the SST turbulence model and experimental inflow conditions upstream of the spray bars and downstream of the heat exchanger. Note that the heat exchanger turbulence along with turbulence caused by the wake of the spray bars and air jets are the most important flow features with respect to obtaining the proper test section turbulence. A min/max technique was used to combine, first, the HX and BARS flow and, finally, HX, BARS, and JETS flows. This approximate linearizing technique is only reasonable if one flow feature dominates the velocity or turbulence variations. The flow solutions including the heat exchanger and the spray bars (HX/BARS) provided good predictions for the test section aerodynamics including the mean velocity and the turbulent kinetic energy distribution and magnitude for the jets-off case. Similarly, the addition of the jet flows to heat exchanger and spray bars flow (HX/BARS/JETS) provided good predictions for the 80 psig jets-on case.

Acknowledgments

This work was supported by NASA John H. Glenn Research Center at Lewis Field. Computer time was furnished by the National Center for Supercomputing Applications. We wish to thank (alphabetically) Pratik Bhattacharjee, Todd Bocksell, Jose Gonsalez, Patrick Hancir, Rajeev Jaiman, Bob Ide, Chris Navarro, Jack Oldenburg, Karthik Srinivasan, and Dennis Yoder for their contributions and support of this investigation.

References

[1] Bragg, M. B., and Khoudadoust, A., "A Study of the Spray Characteristics of a Subsonic Wind Tunnel," *Journal of Aircraft*, Vol. 32, No. 1, 1995, pp. 199–204.

[2] Hancir, P., and Loth, E., "Computations of Droplet Distribution in the IRT," AIAA 99-0097, Jan. 1999.

[3] DeAngelis, B. C., Loth, E., Lankford, D., and Bartlett, C. S., "Computations of Turbulent Droplet Dispersion for Wind Tunnel Test," *Journal of Aircraft*, Vol. 34, No. 2, 1997, pp. 2130–2190.

[4] Irvine, T. B., Kevdzija, S. L., Sheldon, D. W., and Spera, D. A., "Overview of the Icing and Flow Quality Improvements Program for the NASA Glenn Icing Research Tunnel," AIAA Paper 2001-0229, Jan. 2001.

[5] Ide, R. F., and Oldenburg, J. R., "Icing Cloud Calibration of the NASA Glenn Icing Research Tunnel," AIAA Paper 2001-0234, Jan. 2001.

[6] Gonsalez, J. C., Arrington, E. A., and Curry, M. R., "Flow Quality Surveys of the NASA Glenn Icing Research Tunnel (2000 Tests)," AIAA Paper 2001-0232, Jan. 2001.

[7] Bush, R. H., Power, G. D., and Towne, C. E., "WIND: The Production Flow Solver of NPARC Alliance," AIAA Paper 98-0935, Jan. 1998.

[8] Snyder, W. H., and Lumley, J. L., "Some Measurements of Particle Velocity Autocorrelation Functions in a Turbulent Flow," *Journal of Fluid Mechanics*, Vol. 48, 1971, pp. 41–71.

[9] Gonsalez, J. C., Arrington, E. A., and Curry, M. R., "Aero-Thermal Calibration of the NASA Glenn Icing Research Tunnel (2000 Tests)," AIAA Paper 2001-0233, Jan. 2001.